Dissolution DNP using trityl radicals at 7 T field

Author(s):
Jähnig, Fabian; Kwiatkowski, Grzegorz; Däpp, Alexander; Hunkeler, Andreas; Meier, Beat H.; Kozerke, Sebastian; Ernst, Matthias

Publication date:
2017-08

Permanent link:
https://doi.org/10.3929/ethz-b-000190802

Originally published in:
Physical Chemistry Chemical Physics 19(29), https://doi.org/10.1039/c7cp03633g

Funding acknowledgement:
149707 - Method Development for Dissolution Dynamic Nuclear Polarization (SNF)
169879 - Method Development in Solid-State NMR and Dissolution DNP (SNF)

Dissolution DNP using trityl radicals at 7 T field

Fabian Jähnig[1], Grzegorz Kwiatkowski[2], Alexander Däpp[1], Andreas Hunkeler[1], Beat H. Meier[1], Sebastian Kozerke[2], and Matthias Ernst[1]

[1] Physical Chemistry, ETH Zürich, Vladimir-Prelog-Weg 2, 8093 Zürich, Switzerland
[2] Institute for Biomedical Engineering, University and ETH Zürich, Gloriastrasse 35, 8092 Zürich, Switzerland

Abstract

Dissolution DNP has become an important method to generate highly polarized substrates such as pyruvic acid for in-vivo imaging and localized spectroscopy. In a quest to further increase the polarization levels, which is important for in-vivo MRI employing ^{13}C detection, we describe the design and implementation of a new DNP polarizer that is suitable for dissolution operation at 7 T static magnetic field and a temperature of 1.4 K. We describe all important sample preparation steps and experimental details necessary to optimize trityl based samples for use in our polarizer at this higher field. In [1-^{13}C]-pyruvic acid polarization levels of about 56% are achieved, compared to typical polarization levels of about 35-45% at a standard field of 3.4 T. At the same time, the polarization build-up time increases significantly from about 670 s at 3.4 T to around 1300-1900 s at 7 T, depending on the trityl derivate used. We also investigate the effect of adding trace amounts of Gd^{3+} to the samples. While one trityl compound does not exhibit any benefit, the other profits significantly, boosting achievable polarization by 6%.

1. Introduction

The low sensitivity of nuclear-magnetic resonance (NMR) spectroscopy is one of its main limitations in spectroscopy and imaging[1–3]. Research into methods to increase the available polarization has been a common theme since the early days of NMR research[4,5]. Although there is not yet a general method to increase the polarization beyond the thermal-equilibrium value for arbitrary samples, dissolution dynamic polarization (DNP)[6] has become an important technique to generate highly-polarized samples for use in solution-state NMR spectroscopy[7–11] or in-vivo spectroscopy and MRI[12–16]. This has allowed the acquisition of in-vivo images and localized spectra based on ^{13}C chemical shifts with higher signal-to-noise ratio. Currently, the main application of dissolution DNP in this context is the production of highly-polarized [1-^{13}C]-pyruvic acid for use in in-vivo metabolic imaging and spectroscopy of pyruvic acid and its metabolites[17–19].

Despite the widespread use of dissolution DNP, there are currently only two commercial polarizers available, Oxford Hypersense (Oxford Instruments) mainly for spectroscopic applications and SPINlab (GE Healthcare) specifically designed for clinical in-vivo use. Both systems have limitations for basic research which have led to the development of a number of home-built polarizers at various static magnetic fields[20–24]. Originally, most polarizers operated at a static magnetic field of 3.4 T corresponding to an electron Larmor frequency of 94.5 GHz due to the ready availability of microwave sources at this frequency. Going to static magnetic fields higher than 3.4 T has shown the potential to achieve higher polarization values[25–29].

In this publication, we describe the hardware design of a home-built 7 T polarizer suitable for dissolution dynamic nuclear polarization. The design is based on our previous 3.4 T polarizer[30,31] that is in use in our laboratory for basic research[30,32,33] and for in-vivo studies on small animals[34,35] using primarily trityl radicals as electron source.

Trityl radicals have been used for EPR spectroscopy and their structural properties in solution have been studied in detail[36,37]. They are currently the most widely used radicals for direct polarization of ^{13}C nuclei at temperatures around 1 K for producing polarized metabolites for in-vivo applications. Therefore, we characterize the performance of the new 7 T system by investigating the achievable polarization in the solid state of ^{13}C in neat [1-^{13}C]-pyruvic acid doped with two variants of the trityl radical, namely AH111501 and OX063 (see Fig. 1). Additionally, the effect of adding small amounts of gadolinium (Gd^{3+}, Dotarem complex) was investigated for both radicals.

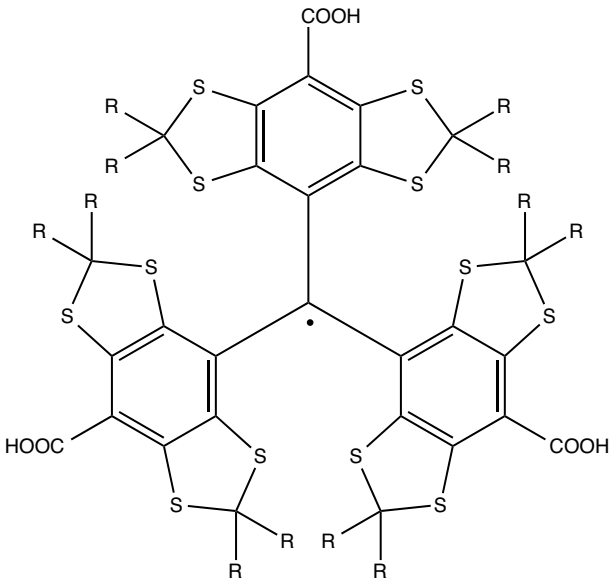

Trityl OX063:
$R=CH_2CH_2OH$

Trityl AH111501:
$R=CH_2CH_2OCH_3$

Figure 1: Schematic drawing of the structure for the two trityl radicals OX063 and AH111501.

2. Hardware and Experiments

2.1 DNP Polarizer and Probe

The design of the polarizer (see schematic drawing in Figure 2) used for the work presented here is based on earlier systems operating at 3.4 T. Details thereof are described in detail elsewhere[38]. The basic design features are shared with home-built DNP systems from other groups[6,21–23,25,39].

The polarizer uses a SpectrostatNMR cryostat (Oxford Instruments) mounted in a 7 T Bruker wide-bore magnet (89 mm) charged to its maximum field (corresponding to 300 MHz ^{1}H resonance frequency). Temperature control is implemented using an ITC-503 controller (Oxford Instruments). For continuous cooling and temperatures above 3 K a membrane pump (Vacuubrand, ME 4NT) is used to transport liquid Helium through the cryogenic system. Lower temperatures can be reached by pumping directly on the cryostat's KF-40 exhaust port using a combination of a roots and a rotary vane pump (WD400, Pfeiffer Vacuum). This mode is time limited to about 2-4 hours, depending on the probe inserted, and operates around a minimum temperature of 1.4 K. A third operating mode is at 4.2 K and ambient pressure, which offers the longest measurement time and uses the least amount of liquid Helium. The various operational modes are described in detail in a previous publication[32].

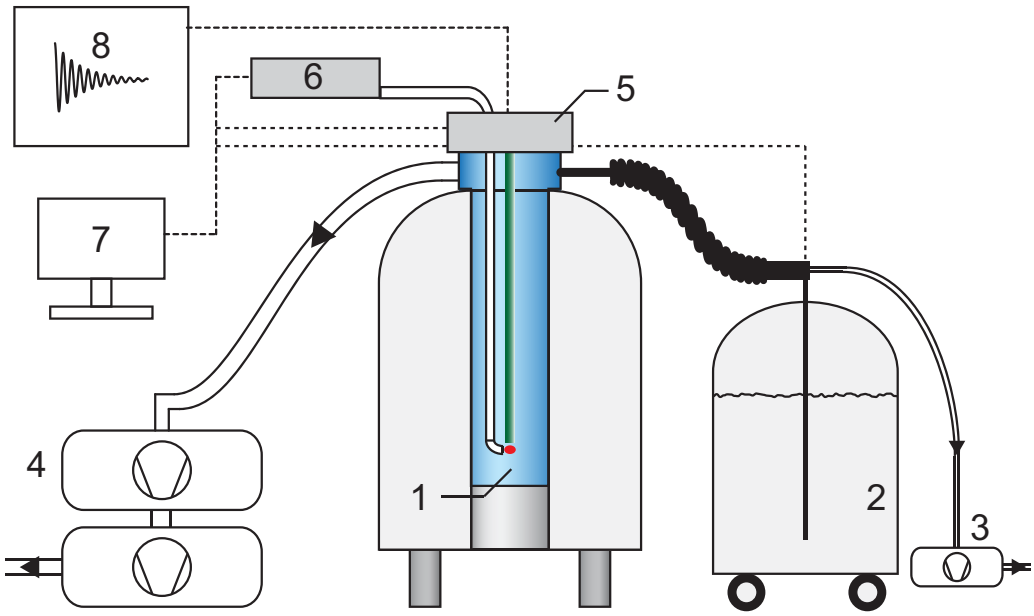

Figure 2: Schematic drawing of the complete polarizer. The cryogenic system consists of a variable temperature cryostat (1), which is cooled with cryogens from an external liquid helium supply dewar (2) via a vacuum-insulated transfer line. Continuous cooling and operation around 3 K is achieved by employing a membrane pump (3) to evacuate the cryostat. Lower temperatures are achieved by using a combination of roots- and rotary vane pumps (4) to pump against the boiling Helium in the cryostat. A home-build probe (5) is mounted inside the cryostat and houses the MW guide connected to the solid-state MW source (6). Monitoring of additional sensors and control of the Helium flow are implemented in LabView software (7), while the NMR data is gathered using a commercial Varian Infinity+ console (8).

Figure 3 shows the general design of the probe with important parts enlarged. It is based on a fiberglass skeleton (18 mm inner diameter, 1 mm wall thickness), which supports the sensors monitoring the DNP experiment as well as the two different NMR inserts. Two temperature sensors (Cernox resistor, Lake Shore Cryotronics Inc.) are used. One is mounted at the bottom of the cryostat, while the other is close to the NMR coil on the bottom baffle of the probe (close to part (4) in Figure 3). Liquid He levels can be monitored using a home-built cylindrical capacitive sensor, which changes its capacitance according to the liquid He level between its electrodes. Additionally, a pressure sensor (Honeywell PX2EG1) is mounted on top of the cryostat to allow monitoring of pump functionality and pressurizing to ambient pressure. Exact pressure values at the sample position cannot be measured since the pressure gradient between top and bottom of the cryostat is not known. To ensure proper positioning of the NMR coil containing the sample with respect to the waveguide antenna position, the probe features a plate at the bottom (see Figure 3(a), part (4)), where a lock-in pin of the NMR insert latches. All sensor data is displayed and recorded using LabVIEW (National Instruments) virtual instruments.

The required microwave irradiation is produced by a solid-state source (VCOM-05/197/50-DD, ELVA) placed near the top of the magnet. It produces microwave irradiation with a maximum power of 52 mW at 196.8-197.8 GHz that is fed into an oversized WR-28 waveguide mounted onto the probe. The waveguide is made of copper for the upper 1/3 of the length while the lower 2/3 are made from stainless steel to limit heat transfer into the sample space. Right above the sample position the rectangular WR-28 waveguide is converted into a circular waveguide

(1.5 mm diameter), with a 90° bend to deliver the MW irradiation to the sample. The attenuation of the microwave power by the waveguide is about -6 dB. Since the sample dimensions are bigger than the wavelength of the MW irradiation a MW antenna is attached at the end of the bend to increase coupling to the sample (see Figure 3(a), part (3)).

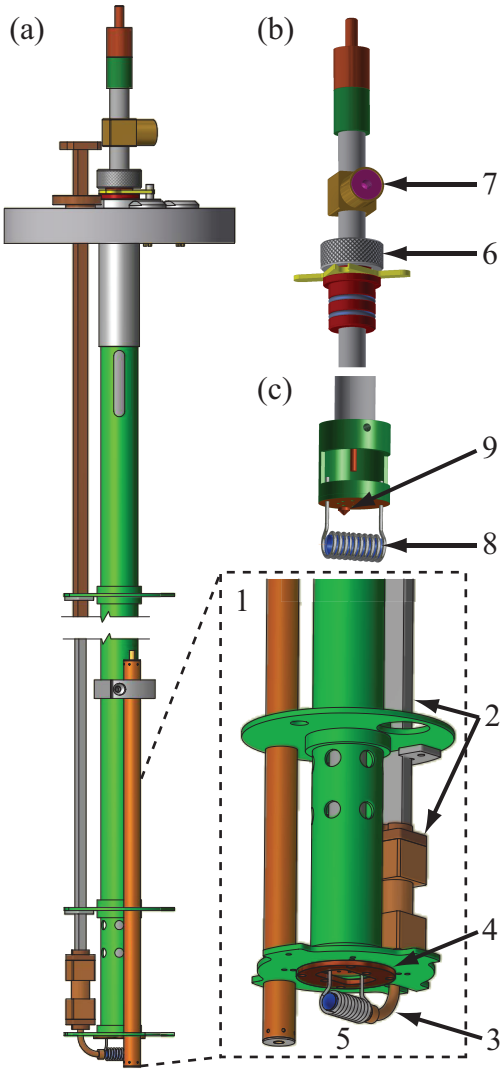

Figure 3: (a) Schematic drawing of the static solid-state DNP probe with the middle section removed. The insert shows a zoom of the lower part where the sample space is located. Its main features are: He sensor (1), MW guide with rectangular-to-circular transition plus 90° bend (2) with antenna (3), positioning plate (4) and NMR coil (5). (b) Top of the vacuum NMR transmission line with orientation slider (6) and pump port (7). (c) Bottom end of the line with the housing for the NMR coil (8) and the fixing pin (9).

Two different NMR transmission lines can be used with the probe depending on the experiments that are performed. First a standard semi-rigid coaxial cable (outer conductor: steel, inner conductor: copper) is available, where at the bottom the outer conductor has been bent in order to clamp the PTFE dielectric to prevent it from sliding out. This transmission line features a solenoid wound from Cu-wire (0.1 mm thick) with 9 windings and 5 mm diameter, which also serves as holder for the sample container. Second a “dielectric-free” transmission line consisting of two concentric steel rods (diameters of 10.5 mm and 4.2 mm and wall thickness of 0.25 mm and 0.3 mm respectively) fixed by polymer spacers glued in between the

two rods has been built. As shown in Figure 3(b) the top part of the dielectric-free transmission line features a pump port to evacuate the space between the two conductors using vacuum as an insulator instead of a dielectric polymer. Figure 3(c) shows the bottom part with the NMR coil and the fixing pin. In this case, the coil is also wound from the same Cu-wire with 7 windings and 5 mm diameter. Both transmission lines are inserted into the cryostat via the inner tube of the skeleton, which allows exchange of samples at ambient pressure but low temperatures (3-4.2 K). For both transmission lines, materials are chosen such that heat transfer to the cold sample space is minimized. In case of the dielectric-free transmission line, this leads to significantly lower He consumption in the non-continuous modes (see above). The available measurement time in those modes is almost doubled to 4 h (single shot) and ~8 h (4.2 K mode) compared to the standard semi-rigid coaxial cable. On the other hand, the dielectric-free transmission line cannot currently tolerate the vibrations from the WD400 pump stand and, therefore, cannot be used at the lowest temperatures, but only down to about 3 K. We are currently working on improving the design such that the vibrations are damped and the use in the low temperature mode becomes possible. With the standard semi-rigid transmission line, the single-shot duration at the lowest temperatures is limited to slightly above two hours. Both transmission lines feature a lock-in pin at the bottom (see Figure 3(c), part (9)), which matches the plate of the fiberglass skeleton ensuring proper positioning of the sample relative to the microwave antenna.

The NMR circuit features two channels tunable in the range of 300 MHz (^{1}H) and 75 MHz (^{13}C). The tuning of the second channel can be switched to a frequency of 46 MHz (^{2}H). Tuning of the channels is achieved by components positioned outside the cryostat at room temperature. Both transmission lines produce rf fields with a nutation frequency in the order of 60-70 kHz for ^{1}H and ^{13}C. NMR experiments are controlled by a Varian Infinity+ spectrometer (Varian Inc.) running Spinsight software.

2.2 Materials

For each sample 200-250 µl of solution were prepared by weighing an appropriate amount of radical (OX063, Oxford Instruments or AH111501) first, then adding the correct amount of [1-^{13}C]-pyruvic acid (Sigma Aldrich) to achieve the desired concentration in the ranges of 15-30 mM. Appropriate amounts of Gd^{3+} (Dotarem, Guerbet, France) were added from a 0.1 M stock solution to achieve concentrations of 1 or 2 mM. The volume effects of both, radical and gadolinium complex solution were neglected in the determination of concentrations. All samples were vortexed and manually centrifuged prior to loading them into the sample container (described in the next section).

2.3 Sample Preparation and Measurement Protocols

As sample container, a Kel-F cylinder (10 mm long, 5 mm diameter, wall thickness 0.5 mm) with one open end was used. It was closed by a Kel-F cap with a small hole to enable pressure release during the loading and unloading of the sample into the polarizer. Loading of the sample container happened in two steps. At first small amounts of liquid sample were frozen by dripping

them into liquid N_2. Subsequently those pellets were transferred into the sample container, which was also submerged in liquid N_2, using tweezers, which were also cooled to liquid N_2 temperature. Finally, the cap of the rotor was pressed on the container by lifting it out of the bath and shortly placing it on the workbench while closing it. Afterwards the container was quickly submerged in liquid N_2 again. The transfer of the pellets and closing of the container were performed as fast as possible, i.e., typically within a few seconds. To load the sample into the precooled cryostat the container was first loaded into the NMR insert of the DNP probe, which was also submerged in liquid N_2, and then inserted into the cryostat. This method of sample preparation is referred to as 'pellet-freezing method' and has been used before for samples using other glassing matrices like glycerol[6] and also pure pyruvic acid[27].

Prior to all measurements, the MW irradiation was optimized for all temperature modes used. From these auxiliary measurements, the optimum irradiation power was determined to 25 mW at 3.4 K and 20 mW at 1.4 K. Higher MW power resulted in lower polarization due to sample heating. This shows that the DNP process in our static probe is not microwave-power limited, at least for this kind of samples.

For each sample, a DNP profile was recorded, to find the optimum irradiation frequency (sweeping the microwave frequency in steps of 0.01 GHz), followed by a buildup/decay experiment to extract T_1 times, at 3.4 K or slightly above. Since ^{13}C T_1 times are very long under typical DNP conditions (1.4 K) and the thermal signal is weak, the thermal equilibrium measurements were recorded at a higher temperature of 3.4 K while the DNP buildup curves were measured at the lowest available temperature of 1.4 K. DNP profiles were measured with a saturation-recovery pulse sequence with relaxation periods of 180-300 s between saturation and acquisition using four low flip-angle (2-3°), phase-cycled pulses.

For buildups and buildup/decay experiments, one FID was acquired using four phase-cycled, low flip-angle pulses (2-3°) every 120 s. In the case of thermal equilibrium measurements, the relaxation delay was set such that the polarization could recover to 99% taking into account the decrease of the polarization by the four pulses. Each thermal equilibrium measurement consisted of 20 FIDs and was started after an initial relaxation delay of 5 T_1. Since the signal in the hyperpolarized state, i.e. during buildup measurements, is very large and the thermal equilibrium signal is much smaller, the dynamic range of the spectrometer was too small to measure both signals with the same settings. Therefore, a different receiver gain and additional attenuation in the receiver path has been used to accommodate the large signal from the hyperpolarized state. Typically, 20 dB attenuation were necessary to avoid saturation of the receiver during buildup measurements. The relative scaling factors of the different receiver settings were checked experimentally.

Independent of the experiment performed, the sample was always fully covered by liquid He at all times to ensure proper cooling of the pellets and a stable temperature in the sample space.

2.4 Data Analysis

All measurements recorded where processed using MATLAB (The Mathworks Inc.). They were phased manually and subsequently Fourier transformed without any additional data processing. To calculate the signal intensities the spectra were first baseline corrected (linear correction) then fit with a Voigt-type line shape, which was then numerically integrated. This way of calculating integrated intensities showed the highest robustness towards baseline distortions. Subsequently, the integrated signal intensity was normalized to the integrated thermal signal after correcting for the difference in temperature (Boltzmann factor), receiver gain and attenuation used in the buildup measurements. Additionally, the enhancement factors were cross checked by comparing the result to the enhancement calculated from integration over the raw data or comparing the first non-distorted point of the FIDs. Enhancements ε, build-up time constants τ and T_1 relaxation times were extracted by mono-exponential fits to the buildup and decay curves. Finally, the enhancement factors were converted to polarization values by multiplying with the Boltzmann polarization at the temperature of the measurement ($P = \tanh\left(h\nu/(2k_{\mathrm{B}}T)\right)$).

3. Results and Discussion

3.1 Reproducibility of Experiments

Glassing of the sample solution is a key point to reach the best possible results, i.e., the highest polarization in the shortest time. This is well known from experiments with other glassing matrices[6], but it is also very important for neat pyruvic-acid samples doped with trityl radicals[27], especially since glassing properties of the solvent cannot be tailored for optimum DNP performance by changing its composition. An alternative approach has been proposed recently where micro crystals are soaked in a solvent doped with the radical or by mechanochemical amorphization[40,41]. It is currently not clear, whether such alternate methods lead to as high polarization levels as dissolving the radical in pyruvic acid. When freezing pyruvic acid samples by insertion into the liquid He bath in the cryostat, measured polarization values were found to be low as well as difficult to reproduce. Reproducibility, i.e., the maximum polarization levels for different experiments on the same sample composition, could be improved by freezing the sample inside its container (slightly different version of the one described in section 2.2) by submerging it in liquid N_2 before inserting the sample into the cold cryostat. Still, the achievable polarization was low compared to published literature values at 3.35 T, 5 T and 6.7 T (see below). There are two possible effects that could responsible for the lower polarization levels in these samples. Either the freezing process is too slow leading to crystalline parts that are not well polarized or the microwave penetration into the block-frozen samples is not as good as in the smaller sized pellets[42]. After changing the preparation procedure to the ‘pellet freezing’ method (see section 2.3), polarization values increased significantly albeit at the cost of increased buildup times. Figure 4 shows the ^{13}C polarization build up under single-shot conditions (1.4 K) for the two different experimental protocols. Freezing the sample into pellets (blue circles) increased the maximum polarization to 55% compared to freezing it as a block in a closed sample container (red squares, 38% polarization).

In addition to the higher polarization, the build-up time increased slightly from 1765 s to 1915 s. In general build-up times at 7 T are significantly longer than at 3.35 T but comparable to published results at 4.6 T[25,26,38].

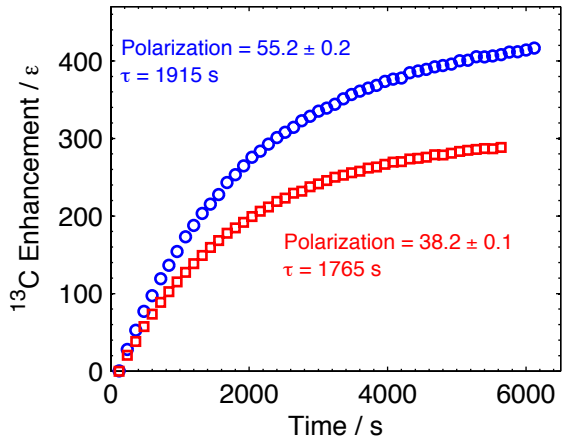

Figure 4: ^{13}C buildup curves for different glassing procedures. Red squares display the buildup on a sample frozen as block in liquid nitrogen, while blue circles show the same sample frozen as pellets. Plotted are enhancements while polarization values and buildup time constants (single fit results) are given as inserts.

The pellet-freezing method has the disadvantage that the sample degrades significantly after a cycle of freezing and warming up, making it a one-time method. Figure 5 shows a measurement of a pellet sample (26 mM AH111501 trityl in neat pyruvic acid, black) compared to a second consecutive measurement of the same sample after warming it up and refreezing it into new pellets (red), resulting in a polarization that is more than 10% lower. A completely fresh sample with the same composition (Figure 5, blue triangles) shows almost identical polarization and buildup time as the first sample.

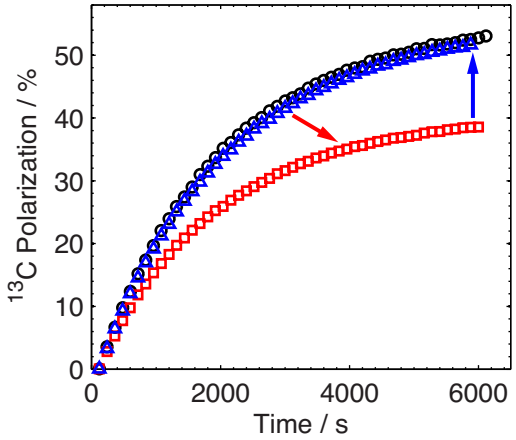

Figure 5: ^{13}C buildup curves for a freshly prepared sample (black circles) and after reusing it (red squares), exhibiting a loss of ca. 10% polarization. Comparing to a different freshly prepared sample of nominally same composition (blue triangles).

3.2 Thermal Equilibrium Data

Measuring thermal-equilibrium data to calibrate the achievable solid-state polarization levels is time consuming (about 8 h measurement time at 3.4 K) due to the long T_1 values and the low thermal-equilibrium signal. Therefore, in many publications only absolute polarization levels

after dissolution are characterized that often show a large spread of values due to variations in the dissolution process. With the "pellet-freezing" method, each series of measurements uses different amounts of sample and would require a thermal-equilibrium spectrum to obtain absolute polarization levels in the solid state.

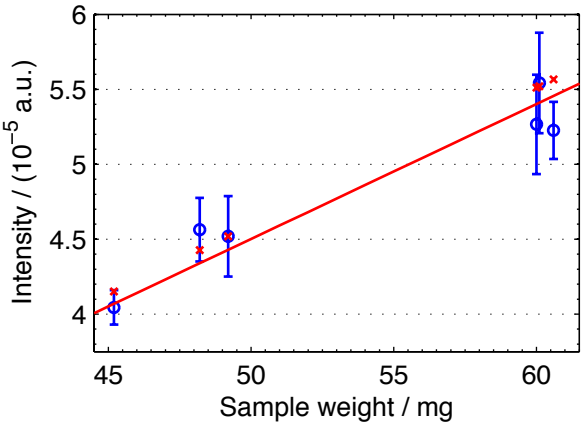

Figure 6: ^{13}C thermal equilibrium signal after waiting 5 T_1 as function of sample weight (blue circles), error bars show standard deviation within each measurement (8 FIDs). Red crosses show values calculated by correction of 1 thermal signal by difference in weight. Red line is a least-squares fit going to zero for zero sample weight.

Since the sample primarily consists of labeled pyruvic acid, the thermal-equilibrium signal without DNP enhancement should be proportional to the weight of the sample. Therefore, one can measure a thermal-equilibrium signal for a given sample composition once and afterwards correct this value for the difference in weight for other samples of the same composition. In Figure 6 the thermal equilibrium signals predicted from the weight of the samples (red crosses, 49 mg sample used as standard) are compared to the measured thermal-equilibrium signals (blue circles) for one selected sample composition and multiple experimental runs. Error bars represent the standard deviation within the thermal measurement composed of 8 FIDs. The red line is a simple linear fit to the data going to zero intensity for zero sample weight (R^2=0.909). Clearly the signal intensity correlates linearly with sample weight, while the predicted values fall within the error bars of the measurements for almost all points. Therefore, the error resulting from calculating the thermal equilibrium signal from the weight of a sample with the same composition is in the same order of magnitude as the error of measuring the thermal-equilibrium polarization.

3.3 DNP Characterization for Trityl AH111501

DNP profiles, normalized to the positive maximum (see Figure 7(a)), show a very similar shape for all measured radical concentrations. Between radical concentrations of 15 mM (black squares) and 30 mM (magenta triangles,) the position of the negative maximum did not change, while the positive maximum moved by about 10 MHz to lower frequency. Additionally, the profiles remain quite symmetric for all concentrations. Optimum irradiation frequencies are in the range of 196.95 to 196.96 GHz for different samples. These values were used for the

measurement of build-up curves under single-shot (1.4 K) conditions.

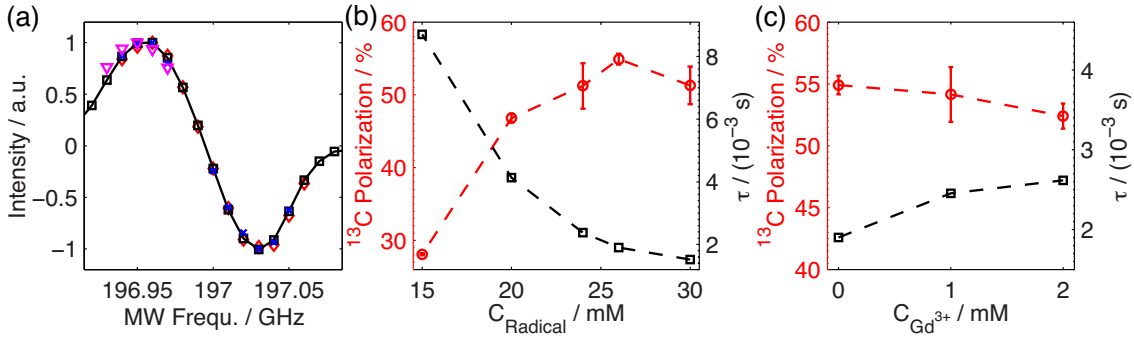

Figure 7: (a) DNP profiles of samples with different concentration of AH111501 (15 mM, black squares to 30 mM, magenta triangles), show a slight broadening of the profile with increasing radical content. (b) polarization and buildup time constants at 1.4 K as function of radical concentration. Samples exhibit a steep increase of polarization to an optimum concentration around 25 mM. Buildup times decrease significantly with higher radical concentration. (c) Addition of trace amounts of Gd3+ does not increase achievable polarization while increasing the buildup time constant. Error bars represent the standard deviation obtained from 3 experiments.

Achievable polarization values show a clear increase for higher radical concentration until they start leveling off at a radical concentration of 24 mM (Figure 7(b)). At 15 mM concentration, which is the typical value used for in-vivo studies at 3.4 T (94.5 GHz), the polarization is almost half (28.1±0.1%) of the maximum reached at 26 mM (54.9±0.8%). A further increase of the radical concentration does not improve polarization values further. At the same time, the build-up time constant τ decreases significantly with increasing radical concentration from 8700±100 s at a radical concentration of 15 mM to 1515±28 s at 30 mM concentration. For the radical concentration with the highest polarization values (26 mM), we find τ = 1900±86 s, which makes it possible to reach the steady-state value after about 2.5 hours.

At lower magnetic fields (3.4 T), the addition of small amounts of a Gd^{3+} complex improves the achievable polarization substantially [43]. In our experiments adding 1-2 mM of a Gd^{3+} complex (Dotarem) shows almost no effect on the achievable polarization if this trityl derivate is used, see Figure 7(c). At a concentration of 2 mM, it actually reduces the maximum polarization slightly to 52±1%. Additionally, adding Gd^{3+} to the sample increases the build-up time significantly to 2600±170 s at this concentration, which is an increase by about 40% compared to a sample without Gd^{3+}. Addition of Dotarem also has a strong effect on the DNP profile (see SI Fig. S1). It becomes asymmetric favoring the negative maximum where ~20% more polarization can be generated compared to the positive maximum.

3.4 DNP Characterization for Trityl OX063

In contrast to the AH111501 trityl, the DNP profiles for OX063 vary stronger with radical concentration. The profiles are again plotted normalized to the positive maximum (see Figure 8(a)). For this radical the DNP profile shows stronger asymmetries and favors the negative maximum for lower radical concentration (15 mM, red diamonds), while it favors the positive maximum for higher radical concentration (30 mM, magenta triangles). In both cases the difference is about 10% comparing positive and negative extrema. As in the case of AH111501,

the position of the maxima shifts as a function of the radical concentration and increasing radical concentration broadens the DNP profile slightly. The positive maximum changes from 196.96 GHz at lower radical concentration (15 mM – red diamonds, 20 mM – black squares) to 196.95 GHz at higher radical concentrations (26 mM – blue crosses, 30 mM – magenta triangles).

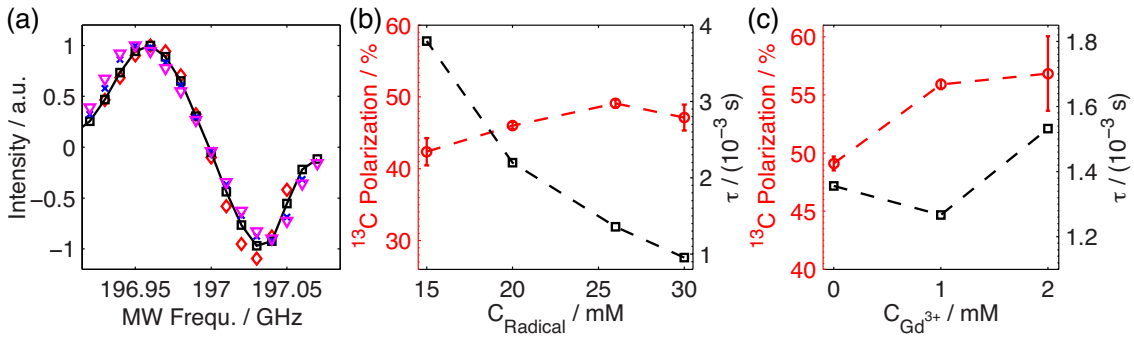

Figure 8: (a) DNP profiles of samples with different concentration of OX063 (15 mM, black squares to 30 mM, magenta triangles), show a slight broadening of the profile with increasing radical content. Additionally, a shift in asymmetry of the profile is seen. (b) polarization and buildup time constants at 1.4 K as function of radical concentration. Samples exhibit a shallow increase of polarization to an optimum concentration around 25 mM. Buildup times decrease significantly with higher radical concentration. (c) Addition of trace amounts of Gd^{3+} does not increase achievable polarization while increasing the buildup time constant. Error bars represent the standard deviation obtained from 3 experiments.

Achievable polarization levels do not depend on the radical concentration as strongly as in the case of AH111501, although there is an increase from 42±2% at 15 mM to 49.1±0.6% at 26 mM concentration. Above this optimum the polarization starts to decrease again with further increase in radical concentration (Figure 8(b)). Build-up time constants (black squares in Figure 8(b)) are significantly shorter when using the OX063 trityl compared to the AH111501. They range from 3800±170 s at the lowest radical concentration to 954±25 s at the highest radical concentration. For the optimum radical concentration, the buildup to the steady state would take about 1.8 h.

In contrast to the AH111501 samples, the addition of small amounts of Gd^{3+} has a strong effect on the achievable polarization in the OX063 samples and also changes the DNP profile significantly (see SI Fig. S2). Adding 1 mM Gd^{3+} to a 25 mM OX063 sample boosts the polarization to 55.9±0.4%, which corresponds to an increase of the polarization by 6% as shown in Figure 8(c). At the same time the build-up time constant decreases to τ = 1267±25 s making the polarization build up faster. Increasing the concentration of Gd^{3+} further does not significantly enhance the polarization on average but mainly increases the spread in the polarization values (see Figure 8(c), last red data point). Interestingly, higher Gd^{3+} concentration also increases the buildup time. In contrast to AH111501, the addition of Dotarem significantly improves the performance of OX063 samples for dissolution DNP.

The origin of the differences in the polarization build up for the two trityl radicals is currently unknown. It has been shown that trityl radicals form oligomers at concentrations above 1 mM in aqueous solutions especially in the presence of other ions like Gd^{3+}.[44,45] Whether such an

oligomer formation is responsible for the differences between the two trityls needs further investigation.

3.5 Performance around 3.4 K

Higher static magnetic fields lead to a saturation of the electron polarization at higher temperatures. Therefore, we have also investigated the achievable polarization at a slightly higher temperature of 3.4 K (see Figure 9, (a) AH111501, (b) OX063). Both radicals exhibit a similar dependence on the radical concentration as at lower temperatures. While there is a steep increase in polarization for the samples doped with AH111501 (Figure 9(a), red circles), there is only a weak dependence on concentration for the OX063 doped samples (Figure 9(b), red circles). In both cases the buildup times (Figure 9, black squares) and spin-lattice relaxation times (Figure 9, blue triangles) decrease steadily with the radical concentration. Although at this temperature the difference in time scales between the two radicals is not as pronounced as at 1.4 K, the OX063 samples still exhibit shorter T_1 and τ.

At a temperature of 3.4 K, the enhancement factors are quite a bit lower, the best samples only achieve around ε = 370 compared to over 400 at 1.4 K. Combined with the lower thermal-equilibrium values at 3.4 K this leads to lower overall polarization values. Still it is possible to reach almost 20% polarization and further improvements using optimized radicals might be possible at this temperature.

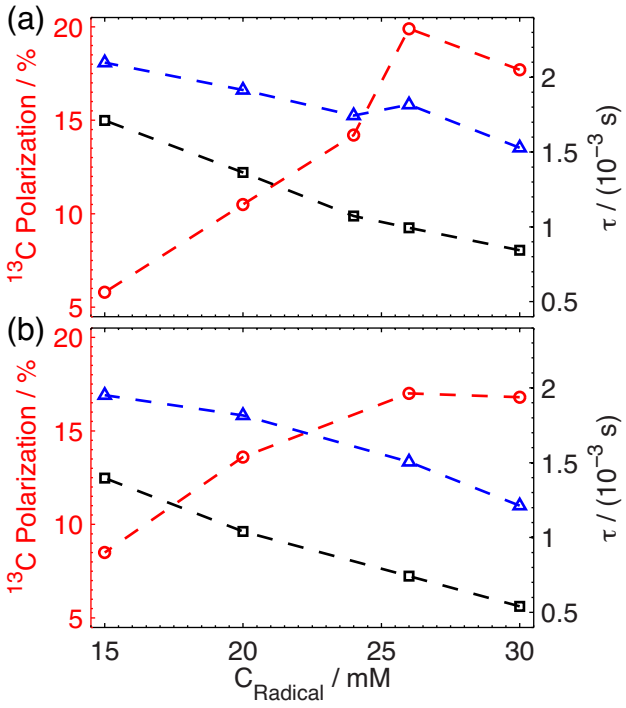

Figure 9: ^{13}C polarization values (red circles), T_1 times (blue triangles) and buildup time constants (black squares) for the same samples as presented in Fig. 7 and 8. (a) displays the data for AH111501 and (b) for OX063.

4. Conclusion

We have described the design of a home-built dissolution DNP polarizer operating at 7 T static magnetic field. The general design follows the same principles as the previously described 3.4 T polarizers with improvements in transmission-line and radio-frequency design. To obtain the highest polarization values, sample freezing of trityl/pyruvate mixtures plays an important role. Only fast freezing of small sample amounts by dripping the solution into liquid Nitrogen ("pellet-freezing method") led to reproducible results.

Comparing the performance of two different trityl radicals (OX063 and AH111501) shows that it is possible to achieve about 56% polarization. However, for OX063, the addition of about 1 mM Gd^{3+} is needed to boost the performance to the same level as for AH111501. For both radicals, the optimum concentration was found to be around 25 mM. The OX063 samples, especially with Gd^{3+}, show substantially shorter buildup times. Taking everything into account, the best sample for in-vivo applications is composed from neat pyruvic acid, doped with 25 mM OX063 and 1 mM Gd^{3+}. It yields the highest polarization values in the shortest amount of time ($P(^{13}C) = 55.9 \pm 0.4\%$, $\tau = 1267 \pm 25$ s). At higher temperatures, i.e., around 3.4 K, almost 20% ^{13}C polarization can be achieved at 7 T static magnetic field.

Comparing our results to literature values at various static magnetic fields (see Table 1), the polarization values reported in this work are significantly higher than what can be achieved at 3.35 T field in our previously built polarizers [31,38]. They are comparable to what has been reported at 4.6 T to 7 T field taking into account the slightly higher temperatures our polarizer operates at. The variation in the buildup times in Table 1 is mainly due to the difference in radical concentration of the optimal sample. Comparing them at the same concentration yields very similar values at field strengths above 4.6 T.

Radical	$c_{rad.}$ [mM]	B_0 [T]	T [K]	$P(^{13}C)$ [%]	$\tau(^{13}C)$ [s]	Ref.
Trityl OX063	15	4.64	1	64/70+	3500	[26]
Trityl OX063	15	4.6	1.15	54.4	3310	[25]
Trityl OX063	15	3.35	1.35	45+	670	[38]
Trityl OX063	15	3.35	1	36	9500	[24]
Trityl OX063	17	7	1.0	60.4	4670	[28]
Trityl AH111501	16	5	0.9	74.7	1104	[27]
Trityl AH111501	26	7	1.4	54.9	1900	this
Trityl OX063	26			55.9+	1360	work

Table 1: Comparison of literature values for direct polarization of ^{13}C using trityl radicals.

+ using added Gd^{3+} usually in concentrations around 1-2 mM

Acknowledgements

Financial support by the Swiss National Science Foundation (SNF grants 200021_149707 and 200020_169879) are gratefully acknowledged.

References

1 A. Abragam, *The Principles of Nuclear Magnetism*, Oxford University Press, 1961.

2 R. R. Ernst, G. Bodenhausen and A. Wokaun, *Principles of Nuclear Magnetic Resonance in One and Two Dimensions*, Clarendon Press Oxford, 1990.

3 P. T. Callaghan, *Principles of Nuclear Magnetic Resonance Microscopy*, Clarendon Press Oxford, 1991.

4 L. T. Kuhn, *Hyperpolarization Methods in NMR Spectroscopy*, 2013, vol. 338.

5 J. H. Ardenkjaer-Larsen, G. S. Boebinger, A. Comment, S. Duckett, A. S. Edison, F. Engelke, C. Griesinger, R. G. Griffin, C. Hilty, H. Maeda, G. Parigi, T. Prisner, E. Ravera, J. Van Bentum, S. Vega, A. Webb, C. Luchinat, H. Schwalbe and L. Frydman, *Angew. Chemie - Int. Ed.*, 2015, **54**, 9162–9185.

6 J. H. Ardenkjaer-Larsen, B. Fridlund, A. Gram, G. Hansson, L. Hansson, M. H. Lerche, R. Servin, M. Thaning and K. Golman, *Proc. Natl. Acad. Sci. U. S. A.*, 2003, **100**, 10158–63.

7 H. Y. Chen, M. Ragavan and C. Hilty, *Angew. Chemie - Int. Ed.*, 2013, **52**, 9192–9195.

8 H. Min, G. Sekar and C. Hilty, *ChemMedChem*, 2015, **10**, 1559–1563.

9 R. Buratto, A. Bornet, J. Milani, D. Mammoli, B. Vuichoud, N. Salvi, M. Singh, A. Laguerre, S. Passemard, S. Gerber-Lemaire, S. Jannin and G. Bodenhausen, *ChemMedChem*, 2014, **9**, 2509–2515.

10 B. Vuichoud, J. Milani, A. Bornet, R. Melzi, S. Jannin and G. Bodenhausen, *J. Phys. Chem. B*, 2014, **118**, 1411–1415.

11 E. Miclet, D. Abergel, A. Bornet, J. Milani, S. Jannin and G. Bodenhausen, *J. Phys. Chem. Lett.*, 2014, **5**, 3290–3295.

12 J. A. M. Bastiaansen, T. Cheng, H. Lei, R. Gruetter and A. Comment, *J. Mol. Cell. Cardiol.*, 2015, **87**, 129–137.

13 H. A. I. Yoshihara, J. A. M. Bastiaansen, C. Berthonneche, A. Comment and J. Schwitter, *AJP Hear. Circ. Physiol.*, 2015, **309**, H2058–H2066.

14 T. Harris, H. Degani and L. Frydman, *NMR Biomed.*, 2013, **26**, 1831–1843.

15 P. Dzien, A. Fages, G. Jona, K. M. Brindle, M. Schwaiger and L. Frydman, *J. Am. Chem. Soc.*, 2016, **138**, 12278–12286.

16 T. B. Rodrigues, E. M. Serrao, B. W. C. Kennedy, D.-E. Hu, M. I. Kettunen and K. M. Brindle, *Nat. Med.*, 2014, **20**, 93–7.

17 S. J. Nelson, J. Kurhanewicz, D. B. Vigneron, P. E. Z. Larson, A. L. Harzstark, M. Ferrone, M. Van Criekinge, J. W. Chang, R. Bok, I. Park, G. Reed, L. Carvajal, E. J. Small, P. Munster, V. K. Weinberg, J. H. Ardenkjaer-larsen, A. P. Chen, R. E. Hurd, L. Odegardstuen, F. J. Robb, J. Tropp and J. A. Murray, *Sci. Transl. Med.*, 2013, **5**, 198ra108.

18 C. H. Cunningham, J. Y. C. Lau, A. P. Chen, B. J. Geraghty, W. J. Perks, I. Roifman, G. A. Wright and K. A. Connelly, *Circ. Res.*, 2016, **119**, 1177–1182.

19 A. P. Chen, J. Y. C. Lau, R. D. A. Alvares and C. H. Cunningham, *Magn. Reson. Med.*, 2015, **73**, 2087–2093.

20 Y. Hovav, D. Shimon, I. Kaminker, A. Feintuch, D. Goldfarb and S. Vega, *Phys. Chem. Chem. Phys.*, 2015, **17**, 6053–6065.

21 S. Jannin, A. Comment, F. Kurdzesau, J. A. Konter, P. Hautle, B. Van Den Brandt and J. J. Van Der Klink, *J. Chem. Phys.*, 2008, **128**, 1–4.

22 T. A. Siaw, A. Leavesley, A. Lund, I. Kaminker and S. Han, *J. Magn. Reson.*, 2016, **264**, 131–153.

23 A. Feintuch, D. Shimon, Y. Hovav, D. Banerjee, I. Kaminker, Y. Lipkin, K. Zibzener, B. Epel, S. Vega and D. Goldfarb, *J. Magn. Reson.*, 2011, **209**, 136–141.

24 J. H. Ardenkjaer-Larsen, A. M. Leach, N. Clarke, J. Urbahn, D. Anderson and T. W. Skloss, *NMR Biomed.*, 2011, **24**, 927–932.

25 L. L. Lumata, R. Martin, A. K. Jindal, Z. Kovacs, M. S. Conradi and M. E. Merritt, *MAGMA*, 2015, **28**, 195–205.

26 H. Johannesson, S. Macholl and J. H. Ardenkjaer-Larsen, *J. Magn. Reson.*, 2009, **197**, 167–175.

27 W. Meyer, J. Heckmann, C. Hess, E. Radtke, G. Reicherz, L. Triebwasser and L. Wang, *Nucl. Instruments Methods Phys. Res. Sect. A Accel. Spectrometers, Detect. Assoc. Equip.*, 2011, **631**, 1–5.

28 H. A. I. Yoshihara, E. Can, M. Karlsson, M. H. Lerche, J. Schwitter and A. Comment, *Phys. Chem. Chem. Phys.*, 2016, **18**, 12409–13.

29 A. Kiswandhi, P. Niedbalski, C. Parish, Q. Wang and L. Lumata, *Magn. Reson. Chem.*, 2017, 1–7.

30 M. Batel, A. D. xe4 pp, A. Hunkeler, B. H. Meier, S. Kozerke and M. Ernst, *Phys. Chem. Chem. Phys.*, 2014, **16**, 21407–21416.

31 M. Krajewski, P. Wespi, J. Busch, L. Wissmann, G. Kwiatkowski, J. Steinhauser, M. Batel, M. Ernst and S. Kozerke, *Magn. Reson. Med.*, 2016, **0**, 1–7.

32 M. Batel, M. Krajewski, A. Däpp, A. Hunkeler, B. H. Meier, S. Kozerke and M. Ernst, *Chem. Phys. Lett.*, 2012, **554**, 72–76.

33 F. Jähnig, G. Kwiatkowski and M. Ernst, *J. Magn. Reson.*, 2016, **264**, 22–29.

34 K. Weiss, A. Sigfridsson, L. Wissmann, J. Busch, M. Batel, M. Krajewski, M. Ernst and S. Kozerke, *NMR Biomed.*, 2013, **26**, 1380–1386.

35 D. O h-Ici, P. Wespi, J. Busch, L. Wissman, M. Krajweski, K. Weiss, A. Sigfridsson, D. Messroghli and S. Kozerke, *Radiology*, 2016, **278**, 742–751.

36 M. K. Bowman, C. Mailer and H. J. Halpern, *J. Magn. Reson.*, 2005, **172**, 254–267.

37 S. N. Trukhan, V. F. Yudanov, V. M. Tormyshev, O. Y. Rogozhnikova, D. V. Trukhin, M. K. Bowman, M. D. Krzyaniak, H. Chen and O. N. Martyanov, *J. Magn. Reson.*, 2013, **233**, 29–36.

38 M. Batel, M. Krajewski, K. Weiss, O. With, A. Däpp, A. Hunkeler, M. Gimersky, K. P. Pruessmann, P. Boesiger, B. H. Meier, S. Kozerke and M. Ernst, *J. Magn. Reson.*, 2012, **214**, 166–174.

39 A. A. Smith, B. Corzilius, J. A. Bryant, R. Derocher, P. P. Woskov, R. J. Temkin and R. G. Griffin, *J. Magn. Reson.*, 2012, **223**, 170–179.

40 E. Elisei, M. Filibian, P. Carretta, S. Colombo Serra, F. Tedoldi, J. F. Willart, M. Descamps and a. Cesàro, *Chem. Comm.*, 2015, **51**, 2080–2083.

41 X. Ji, A. Bornet, B. Vuichoud, J. Milani, D. Gajan, A. J. Rossini, L. Emsley, G. Bodenhausen and S. Jannin, *Nat. Commun.*, 2017, **8**, 13975.

42 B. Lama, J. H. P. Collins, D. Downes, A. N. Smith and J. R. Long, *NMR Biomed.*, 2016, **29**, 226–231.

43 L. L. Lumata, M. E. Merritt, C. R. Malloy, A. D. Sherry and Z. Kovacs, *J. Chem. Phys. A*, 2012, **116**, 5129–38.

44 I. Marin-Montesitos, J. C. Paniagua, M. Vilaseca, A. Urtizberea, F. Luis, M. Feliz, F. Lin, S. Van Doorslaer and M. Pons, *Phys. Chem. Chem. Phys.*, 2015, **17**, 5785–5794.

45 I. Marin-Montesinos, J. C. Paniagua, A. Peman, M. Vilaseca, F. Luis, S. Van Doorslaer and M. Pons, *Phys. Chem. Chem. Phys.*, 2016, **18**, 3151–3158.